

# Open-Shell Donor–Acceptor Conjugated Polymers with High Electrical Conductivity

Lifeng Huang, Naresh Eedugurala, Anthony Benasco, Song Zhang, Kevin S. Mayer, Daniel J. Adams, Benjamin Fowler, Molly M. Lockart, Mohammad Saghaezhian, Hamas Tahir, Eric R. King, Sarah Morgan, Michael K. Bowman, Xiaodan Gu, and Jason D. Azoulay\*

Conductive polymers largely derive their electronic functionality from chemical doping, processes by which redox and charge-transfer reactions form mobile carriers. While decades of research have demonstrated fundamentally new technologies that merge the unique functionality of these materials with the chemical versatility of macromolecules, doping and the resultant material properties are not ideal for many applications. Here, it is demonstrated that open-shell conjugated polymers comprised of alternating cyclopentadithiophene and thiadiazoloquinoxaline units can achieve high electrical conductivities in their native “undoped” form. Spectroscopic, electrochemical, electron paramagnetic resonance, and magnetic susceptibility measurements demonstrate that this donor–acceptor architecture promotes very narrow bandgaps, strong electronic correlations, high-spin ground states, and long-range  $\pi$ -delocalization. A comparative study of structural variants and processing methodologies demonstrates that the conductivity can be tuned up to  $8.18 \text{ S cm}^{-1}$ . This exceeds other neutral narrow bandgap conjugated polymers, many doped polymers, radical conductors, and is comparable to commercial grades of poly(styrene-sulfonate)-doped poly(3,4-ethylenedioxythiophene). X-ray and morphological studies trace the high conductivity to rigid backbone conformations emanating from strong  $\pi$ -interactions and long-range ordered structures formed through self-organization that lead to a network of delocalized open-shell sites in electronic communication. The results offer a new platform for the transport of charge in molecular systems.

(opto)electronic functionalities not accessible using traditional materials. Widespread efforts in scientific and engineering disciplines have led to the advancement of synthetic, organic-based conductors such as carbon nanotubes, graphene, graphene nanoribbons (GNRs), charge-transfer complexes, and neutral radical species.<sup>[1–7]</sup> Conductive polymers (CPs) offer key advantages such as the possibility to tailor molecular and electronic structure through chemical synthesis and enable low-temperature fabrication approaches amenable to large areas and various form factors. Prototypical CPs such as poly(3,4-ethylenedioxythiophene) require doping to achieve high electrical conductivity ( $\sigma$ ), a process that results in mobile carriers of electric charge in the form of polarons and bipolarons. These quasiparticles represent coulombically bound charge and counterion pairs with  $\sigma$  and the mode of transport varying based on the type of dopant, doping level, and interrelated structural, morphological, and electronic properties.<sup>[8–12]</sup> Worldwide efforts have led to impressive values for  $\sigma$ ,<sup>[8,11,13]</sup> however, doping leads to high chemical reactivity, material and device instability, processing


## 1. Introduction

Emerging technologies require versatile conductors that offer mechanical properties, geometric forms, and engineered

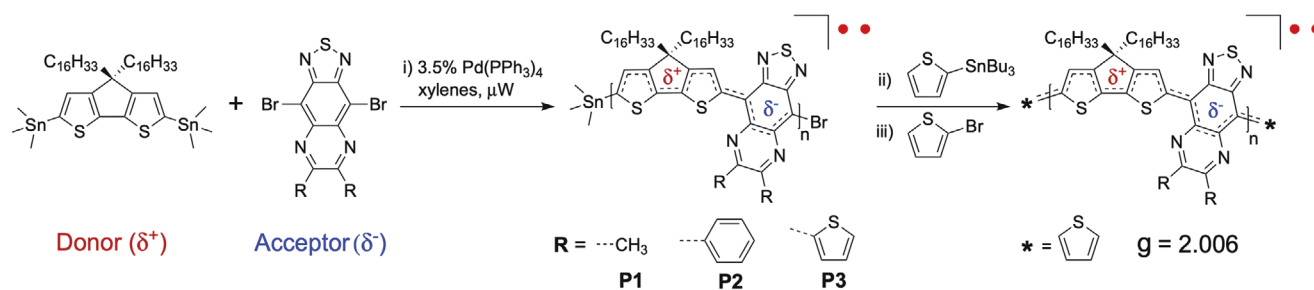
and performance variability, and incompatibility with various substrates and electronic components. As such, there has been a long-standing interest in neutral narrow bandgap conjugated polymers that promote high  $\sigma$  in their native form; however,

Dr. L. Huang, Dr. N. Eedugurala, A. Benasco, S. Zhang, K. S. Mayer, Dr. D. J. Adams, H. Tahir, E. R. King, Prof. S. Morgan, Prof. X. Gu, Prof. J. D. Azoulay  
Center for Optoelectronic Materials and Devices  
School of Polymer Science and Engineering  
The University of Southern Mississippi  
Hattiesburg, MS 39406, USA  
E-mail: jason.azoulay@usm.edu

B. Fowler, Dr. M. M. Lockart, Prof. M. K. Bowman  
Department of Chemistry  
The University of Alabama  
Tuscaloosa, AL 35487-0336, USA  
Dr. M. Saghaezhian  
Department of Physics and Astronomy  
Louisiana State University  
Baton Rouge, LA 70803, USA

 The ORCID identification number(s) for the author(s) of this article can be found under <https://doi.org/10.1002/adfm.201909805>.

DOI: 10.1002/adfm.201909805



**Scheme 1.** Synthesis of open-shell donor–acceptor conjugated polymers using a Stille cross-coupling copolymerization. i) **P1**: 120 °C for 5 min, 140 °C for 5 min, 170 °C for 20 min; **P2** and **P3**: 120 °C for 5 min, 140 °C for 5 min, 170 °C for 60 min, 190 °C for 10 min; ii) 0.25 equivalents (relative to acceptor) of 2-(tributylstannyl)thiophene in 1 mL xylenes, then 100 °C for 12 h; iii) 10 equivalents (relative to acceptor) of 2-bromothiophene, then 100 °C for 12 h.

decades of research have met with limited success, with  $\sigma$  ranging from  $\approx 10^{-10}$  to  $10^{-2}$  S cm $^{-1}$ .<sup>[4,14–16]</sup>

There remains a number of significant challenges to overcome the need for chemical doping in organic materials systems. Controlling the bandgap at low energies would enable the promotion of free carriers by thermal activation, but this remains a challenge owing to the absence of design rules that connect chemical, electronic, and structural heterogeneities with the degree of electronic correlation and energetic disorder in these materials. Neutral radical conductors with unpaired electrons mediate charge and spin transport through open-shell sites,<sup>[1,2,17–19]</sup> but very few are persistent, are not Mott insulators, and show the electronic dimensionality necessary to facilitate long-range transport.<sup>[20]</sup> Unpaired electrons manifest from resonating electronic states in open-shell diradicals, but the high reactivity of these species necessitates kinetic stabilization through steric protection, masking intermolecular  $\pi$ - $\pi$  and orbital interactions that facilitate charge transport.<sup>[20–22]</sup> Extension of the  $\pi$ -system affords a reduction in the bandgap, enhanced  $\sigma$ , open-shell character, and thermodynamic stabilization through long-range  $\pi$ -delocalization, as evident in polycyclic aromatic hydrocarbons, nanographenes, and GNRs.<sup>[3,4,15,21]</sup> However, bottom-up chemical approaches to access these materials and control their properties continue to meet with considerable difficulties and their high reactivity limits their study to surface-mediated syntheses under ultrahigh vacuum conditions.<sup>[21,23–25]</sup>

While most conventional conjugated polymers are closed-shell species accommodating their  $\pi$ -electrons in bonding orbitals, donor-acceptor (DA) copolymers with quinoidal character, extended  $\pi$ -systems, and narrow bandgaps demonstrate open-shell electronic structures.<sup>[4,26–29]</sup> We previously demonstrated that DA copolymers based on cyclopentadithiophene-thiadiazoloquinoxaline (CPDT-TQ) frameworks exhibit very narrow bandgaps ( $0.5 \text{ eV} < E_g < 1 \text{ eV}$ ), room-temperature conductivities ( $\sigma_{\text{RT}}$ ) of  $\approx 10^{-2}$ – $10^{-3} \text{ S cm}^{-1}$ , and controlled spin multiplicities, emanating from a high degree of electronic coherence along the  $\pi$ -conjugated backbone.<sup>[26,27]</sup> In these materials, narrow bandgaps increase configuration mixing, while extension of the  $\pi$ -system promotes topological localization of  $\alpha$  and  $\beta$  singly occupied molecular orbitals to opposite sides of the macromolecule, diminishing the covalency of the ground state and increasing the diradical character ( $\gamma$ ). Both the singlet ( $S = 0$ ) and triplet ( $S = 1$ ) states are nearly degenerate and there is extensive delocalization, promoting thermodynamic stabilization, unpaired spin densities, and electrical conductivity.

These results, and an incipient body of literature, are consistent with the emergence of open-shell DA polymers with strong  $\pi$ -correlations that drive the formation of diverse electronic states and open opportunities for the development of new conductive materials. There remains a critical need for bottom-up chemical approaches that combine bandgap and electronic structure control, and which can also provide detailed insight into how conformational, morphological, and transport phenomena relate in emerging correlated systems. Here, we demonstrate that open-shell conjugated polymers can achieve high electrical conductivities in their native “undoped” form.

## 2. Results and Discussion

We examined a series of open-shell DA polymers with CPDT–TQ backbones, as shown in **Scheme 1**. Salient design features include a CPDT donor, which raises the highest occupied molecular orbital (HOMO) and promotes rigid backbones, while linear  $\text{—C}_{16}\text{H}_{33}$  side chains provide solubility.<sup>[30,31]</sup> Strong, proquinoidal TQ acceptors lower the lowest unoccupied molecular orbital (LUMO) and facilitate strong intramolecular interactions, promoting very narrow bandgaps, a quinoidal bonding pattern, backbone rigidity, and unpaired spin densities.<sup>[26,27]</sup> Substitution of the TQ acceptor with methyl (**P1**), phenyl (**P2**), and thiophene (**P3**) moieties affords the capability to fine-tune structural and electronic features. The polymers were synthesized using a modified microwave-assisted Stille cross-coupling copolymerization between (4,4-dihexadecyl-4*H*-cyclopenta[2,1-*b*:3,4-*b'*]dithiophene-2,6-diyl)bis(trimethylstannane)<sup>[32]</sup> and 4,9-dibromo-6,7-dimethyl-[1,2,5]thiadiazolo[3,4-*g*]quinoxaline<sup>[33]</sup> for **P1**, 4,9-dibromo-6,7-diphenyl-[1,2,5]thiadiazolo[3,4-*g*]quinoxaline<sup>[34]</sup> for **P2**, and 4,9-dibromo-6,7-di(thiophen-2-yl)-[1,2,5]thiadiazolo[3,4-*g*]quinoxaline<sup>[35]</sup> for **P3**. We used  $\text{Pd}(\text{PPh}_3)_4$  as the catalyst (3.5 mol%) in xylenes and a reaction time of 30 min for **P1**, and 80 min for **P2** and **P3**, followed by in situ chain-end functionalization with thiophenes. End functionalization has been shown to improve purity, stability, and ordering.<sup>[30,31]</sup> Substantial efforts were dedicated to obtain **P1–P3** in sufficiently high and similar number average molecular weights ( $M_n$ ) in order to compare their properties and performance. Gel permeation chromatography at 55 °C in chloroform ( $\text{CHCl}_3$ ) showed a  $M_n$  of 58.8, 53.4, and 54.0 kg  $\text{mol}^{-1}$  and dispersity ( $\bar{D}$ ) of 1.20, 2.00, and 2.04 for **P1–P3**, respectively.

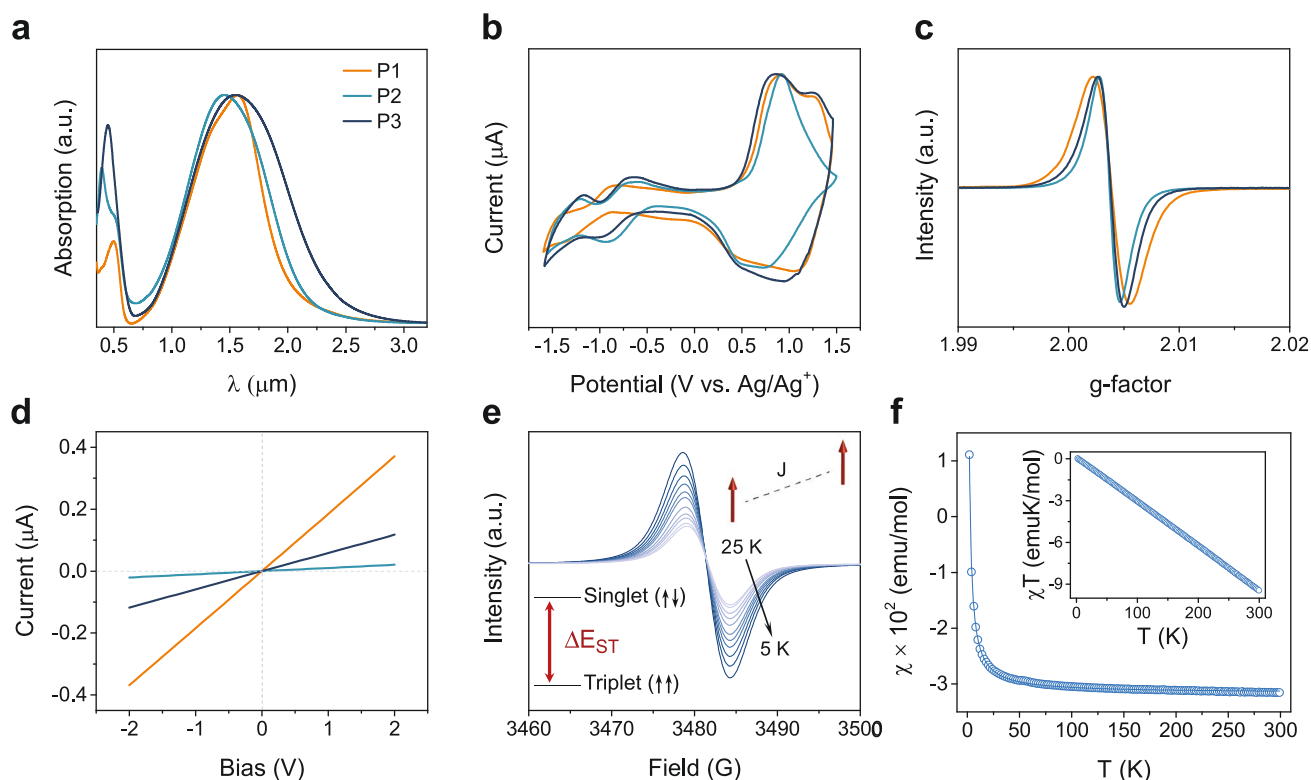


**Figure 1.** Solid-state properties. a) Absorption spectra of thin films spin-coated from chlorobenzene solutions onto quartz substrates. b) Cyclic voltammetry profiles indicating oxidation and reduction peaks. c) EPR (X-band) spectra of the polymers at room temperature. d) Current–voltage characteristics comparing spin-coated films. e) EPR spectra of **P1** from 25 to 5 K used for the temperature-dependent fit to the Bleaney–Bowers equation with a singlet–triplet energy splitting ( $\Delta E_{ST}$ ) of  $7.81 \times 10^{-3}$  kcal mol $^{-1}$ . The inset is an illustration of intramolecular exchange coupling ( $J$ ) and  $\Delta E_{ST}$ . f) SQUID magnetometry of a solid-state **P1** sample with magnetic susceptibility ( $\chi$ ) versus temperature ( $T$ ), from 2 to 300 K fit to a modified Curie law (blue line) with the temperature dependence of  $\chi T$  (inset).

Thin films of the polymers show absorption profiles with maxima ( $\lambda_{\text{max}}$ ) of 1.60  $\mu\text{m}$  (**P1**), 1.45  $\mu\text{m}$  (**P2**), and 1.66  $\mu\text{m}$  (**P3**) and relatively sharp band-tail characteristic of undoped polymers (Figure 1a).<sup>[26]</sup> The optical bandgap ( $E_{\text{g}}^{\text{opt}}$ ) of **P1** is 0.57 eV, as estimated from the absorption onset of the thin film. Cyclic voltammetry shows that the HOMO is located at  $-4.93$  eV and the LUMO at  $-3.90$  eV, which gives an electrochemical bandgap ( $E_{\text{g}}^{\text{elec}}$ ) of 1.03 eV (Figure 1b and Table S1 (Supporting Information)). The effect of substitution of the TQ acceptors indicates different levels of electronic coupling. In comparison to **P1**, a reduction in aggregation is evident in **P2** and **P3**, as noted by the broad featureless absorption profiles and the absence of a shoulder in the short-wavelength infrared region (Figure 1a). The electrochemical characteristics of **P2** and **P3** (**P2**:  $E_{\text{HOMO}} = -5.06$  eV;  $E_{\text{LUMO}} = -4.19$  eV;  $E_{\text{g}}^{\text{elec}}$  of 0.87 eV; **P3**:  $E_{\text{HOMO}} = -4.95$  eV;  $E_{\text{LUMO}} = -4.15$  eV;  $E_{\text{g}}^{\text{elec}}$  of 0.80 eV) demonstrate that substituents can also modify the frontier orbital energetics (Figure 1b). Electron paramagnetic resonance (EPR) spectroscopy at room temperature displayed broad single lines at a  $g$ -factor ( $g$ ) of 2.006 with spin concentrations of  $6.03 \times 10^{22}$  (**P1**),  $6.68 \times 10^{22}$  (**P2**), and  $5.23 \times 10^{22}$  spins mol $^{-1}$  (**P3**) and similar dipolar spectroscopic properties (Figure 1c). The temperature-dependent EPR of **P1** displayed an increase in intensity with cooling, indicating a paramagnetic ground state (Figure 1e). Fitting of the data to the Bleaney–Bowers equation in the 5–20 K

range revealed a very narrow singlet–triplet energy gap ( $\Delta E_{ST}$ ) of  $7.81 \times 10^{-3}$  kcal mol $^{-1}$  ( $J = 1.37$  cm $^{-1}$ ), indicating weak ferromagnetic coupling (Figure S5, Supporting Information). These data are consistent with superconducting quantum interference device (SQUID) magnetometry measurements in which a diamagnetic state is thermally populated with the magnetic susceptibility ( $\chi$ ) decreasing sharply as the temperature is increased from 2 to 50 K and remaining relatively flat across a wide temperature range (50–300 K) (Figure 1f). The  $\chi T$  versus  $T$  plot (Figure 1f, inset) has a linear temperature dependence with a negative slope, consistent with diamagnetic behavior.

Charge transport measurements were obtained by spin-coating films from  $\text{CHCl}_3$  solutions (10 mg mL $^{-1}$ ) onto pre-patterned Au electrodes. Two-point probe measurements showed linear current–voltage ( $I$ – $V$ ) characteristics with  $\sigma_{\text{RT}} = 3.05 \times 10^{-2}$ ,  $9.25 \times 10^{-5}$ , and  $4.13 \times 10^{-4}$  S cm $^{-1}$  for **P1**–**P3**, respectively (Figure 1d). The Ohmic transport in these materials can be associated with the low energetic barrier for thermal excitation of free carriers and extensive delocalization.<sup>[3,4,14,15,36]</sup> Grazing-incidence wide-angle X-ray scattering (GIWAXS) profiles for the spin-coated films demonstrate that **P1** is weakly crystalline while **P2** and **P3** are nearly amorphous (Figure 2a,b). The presence of low  $q$  peaks ( $\approx 0.25$  Å $^{-1}$ , 25.13 Å) with no higher-order Bragg reflections for all three polymers is due to weakly ordered lamellar stacking, as indicated from

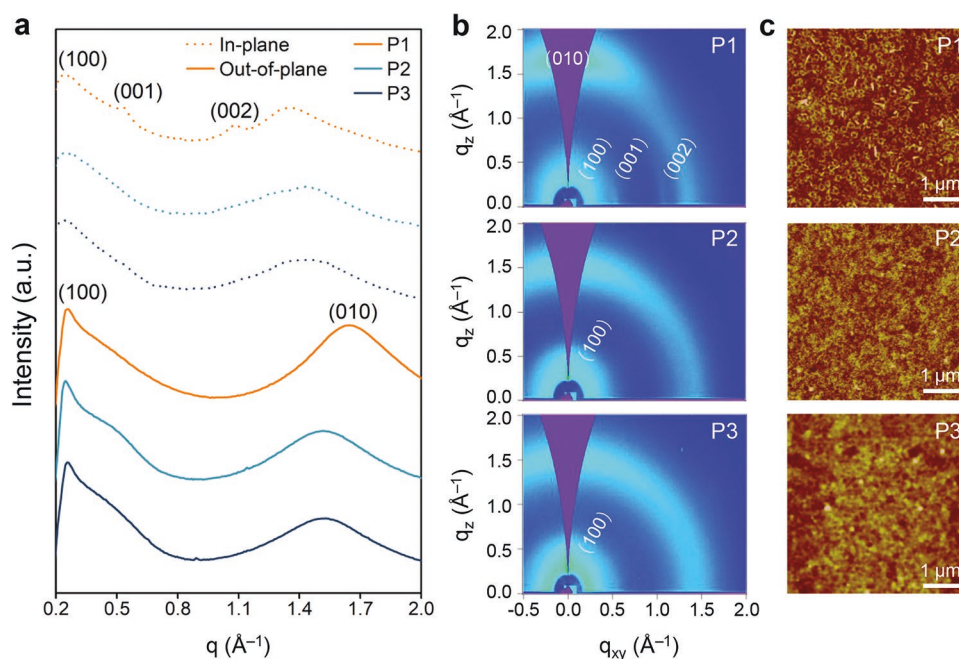


**Figure 2.** Morphological studies of the spin-coated **P1–P3** polymer thin films. a) 1D line cuts of the integrated in-plane and out-of-plane GIWAXS profiles illustrating distinct backbone packing and  $\pi$ – $\pi$  stacking for **P1** and weakly ordered lamellar stacking for **P2** and **P3**. b) The corresponding 2D GIWAXS profiles. c) AFM height images ( $5 \times 5 \mu\text{m}$ ) demonstrating the semicircular self-assembled nanostructures associated with the **P1** film and relatively smooth surfaces with small granular aggregates from **P2** and **P3** films.

the (100) scattering peaks from the polymer side chains. **P1** shows additional in-plane peaks at  $q \approx 0.54 \text{ \AA}^{-1}$  ( $d \approx 11.64 \text{ \AA}$ ) and  $q \approx 1.07 \text{ \AA}^{-1}$ , which can be attributed to polymer backbone packing (001) and (002), respectively. The broad peak from  $q \approx 1.20$  to  $1.70 \text{ \AA}^{-1}$  is ascribed to amorphous scattering from disordered regions within the **P2** and **P3** films. By contrast, a well-defined out-of-plane peak at  $q \approx 1.65 \text{ \AA}^{-1}$  corresponds to an intermolecular ordering ( $\pi$ – $\pi$  stacking) distance of  $\approx 3.81 \text{ \AA}$  with a face-on arrangement for **P1**. As seen in atomic force microscopy (AFM) images, spin-coated films of **P1** show semicircular self-assembled nanostructures  $\approx 100 \text{ nm}$  in diameter with root mean square (RMS) roughness of  $1.62 \text{ nm}$  that establish an interconnected polymer network resulting in higher  $\sigma_{\text{RT}}$  (Figure 2c and Figure S9 (Supporting Information)).<sup>[37]</sup> By contrast, **P2** and **P3** films exhibit relatively smooth surfaces (RMS roughness of  $0.40$  and  $0.32 \text{ nm}$ , respectively) with small granular aggregates  $5$ – $10 \text{ nm}$  in size randomly distributed across the surface. While different  $\sigma_{\text{RT}}$  spreading over three orders of magnitude reflect different levels of electronic coupling and disorder arising from the presence of bulky aryl substituents on the TQ acceptors, values for  $\sigma_{\text{RT}}$  agree with EPR linewidths ( $\Delta H$ ) obtained from solid-state spectra at room temperature of **P1** ( $5.87 \text{ G}$ ) > **P3** ( $4.50 \text{ G}$ ) > **P2** ( $3.91 \text{ G}$ ) (Figure 1c). The spin–lattice relaxation time ( $T_1$ ) and the spin–spin relaxation time ( $T_2$ ) are related to  $\Delta H$  through the equation  $\Delta H = 1/T_2 + 1/2T_1$ . At room temperature, the fast spin–lattice relaxation is dominant, following an Elliott–Yafet like mechanism. As such, a decrease in the spin relaxation time occurs when more efficient pathways are present and wavefunctions can oscillate along a more rigid backbone or through enhanced  $\pi$ – $\pi$  interactions (Figure 2a,b).<sup>[38]</sup>

Spin-coating often results in rapid solvent removal and kinetically quenched, poorly ordered films. To further increase  $\sigma_{\text{RT}}$ , we evaluated a solvent vapor-assisted slow-drying technique to improve chain organization through reducing the solvent evaporation rate and improving the chain mobility.<sup>[39]</sup>  $\text{CHCl}_3$  solutions ( $1.8 \text{ mg mL}^{-1}$ ) were drop-cast onto pre-patterned Au electrodes in a closed container saturated with a good solvent vapor ( $\text{CHCl}_3$ ) or a poor solvent vapor (hexanes) and allowed to dry (see the Supporting Information). For **P1** films slow-dried in  $\text{CHCl}_3$ ,  $\sigma_{\text{RT}}$  is enhanced more than 100-fold from an average value of  $3.05 \times 10^{-2}$  to  $2.46 \text{ S cm}^{-1}$ , with high performing devices exceeding  $8 \text{ S cm}^{-1}$  (Figure S10d, Supporting Information), while  $\sigma_{\text{RT}}$  is decreased to  $1.91 \times 10^{-5} \text{ S cm}^{-1}$  for films slow-dried in hexanes. A similar trend is evident for **P2** and **P3**, with  $\sigma_{\text{RT}}$  of  $2.89 \times 10^{-3} \text{ S cm}^{-1}$  for **P2** films slow-dried in  $\text{CHCl}_3$  and  $3.23 \times 10^{-5} \text{ S cm}^{-1}$  for films slow-dried in hexanes, while **P3** films slow-dried in  $\text{CHCl}_3$  result in  $\sigma_{\text{RT}}$  of  $3.75 \times 10^{-3} \text{ S cm}^{-1}$  and  $7.46 \times 10^{-5} \text{ S cm}^{-1}$  for films slow-dried in hexanes (Figure 3a and Figure S10 (Supporting Information)). To identify correlations between  $\sigma_{\text{RT}}$  and the carrier mobility ( $\mu$ ) as a function of processing conditions, we fabricated field-effect transistors (FETs) with a  $\text{Si/SiO}_2$  ( $300 \text{ nm}$ )/octadecyltrichlorosilane/Au ( $60 \text{ nm}$ )/polymer architecture. Figure 3b summarizes the FET-measured  $\mu$  for **P1–P3**, extracted from the linear region of the transfer curves. An examination of the transport properties for various processing conditions illustrates that  $\mu$  increases with  $\sigma$  in the presence of  $\text{CHCl}_3$  vapor and decreases when hexane vapor is used. The average mobilities obtained from films slow-dried in  $\text{CHCl}_3$  are  $1.75 \times 10^{-1}$  (**P1**),  $4.50 \times 10^{-4}$  (**P2**), and  $1.95 \times 10^{-3} \text{ cm}^2 \text{ V}^{-1} \text{ s}^{-1}$  (**P3**). The carrier concentration for all devices was calculated from the equation  $\sigma = nq\mu$ , where

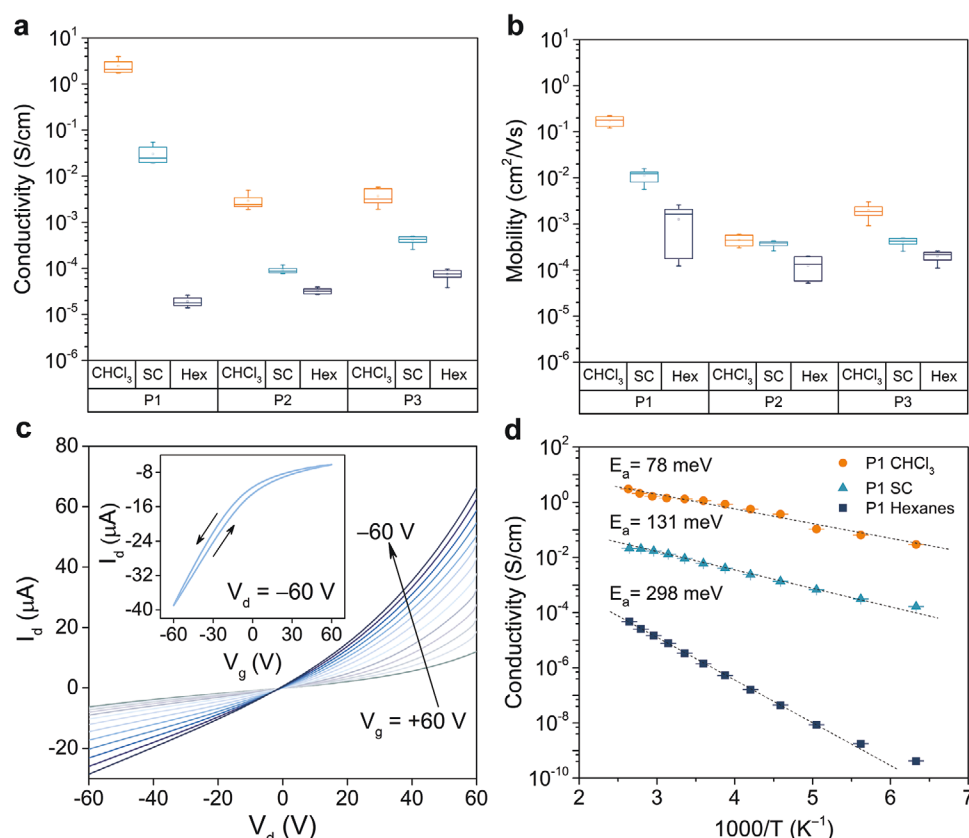


**Figure 3.** Charge transport properties of the polymers compared using different processing conditions. a) Summary of electrical conductivities obtained from two-point probe measurements (−2 to 2 V) comparing 10 independent devices of spin-coated (SC) and slow-dried films using chloroform (CHCl<sub>3</sub>) and hexanes (Hex) (channel length (*L*) = 30–80 μm, width (*W*) = 1 mm). b) FET-measured hole mobilities of the corresponding films extracted from the linear region of the transfer curves at a drain voltage of −60 V using a bottom contact device architecture of octadecyltrichlorosilane (CH<sub>3</sub>(CH<sub>2</sub>)<sub>17</sub>SiCl<sub>3</sub>)-treated Si/SiO<sub>2</sub> (300 nm) substrates and Au (60 nm) electrodes (*L* = 30–80 μm, *W* = 1 mm). c) Representative FET output characteristics (inset: transfer curve) of a spin-coated **P1** film. d) Temperature-dependent conductivity measurements (160–380 K) of **P1** films cast from different processing conditions. Error bars represent the standard deviation of three iterative measurements.

$q$  is the elementary charge, and  $n$  is the carrier concentration (Table S2, Supporting Information), indicating a proportional increase of  $\sigma$  with  $n$ . The calculated carrier concentration in these systems ranges from  $10^{17}$  to  $10^{19}$  cm<sup>−3</sup>, which is comparable to high performing heavily doped systems.<sup>[40]</sup> In all samples, the output curves (Figure 3c and Figure S11 (Supporting Information)) do not illustrate distinct linear and saturation regions at varying gate voltages ( $V_g$ ) and the drain current ( $I_d$ ) increased linearly with drain voltage ( $V_d$ ) from −60 to 60 V. The transfer curves (Figure 3c, inset and Figure S11, inset (Supporting Information)) do not demonstrate any off-state, indicating the presence of free carriers and reducing the magnitude of the field effect. Variable temperature measurements (160–380 K) of **P1** films across different processing conditions demonstrate that  $\sigma$  increases with temperature (Figure 3d) following a thermally activated relation  $\sigma(T) = \sigma_0 \exp(-E_a/k_B T)$ , where  $\sigma_0$  is a pre-exponential factor,  $E_a$  is the activation energy,  $k_B$  is the Boltzmann constant, and  $T$  denotes the temperature. Values for  $E_a$  of 78 meV (slow-dried in CHCl<sub>3</sub>) < 131 meV (spin-coating) < 298 meV (slow-dried in hexanes) are consistent with the conductivity and mobility measurements (Table S2, Supporting Information) and are indicative of a reduction in the energetic barrier for charge transport.<sup>[26]</sup>

The effects of structural features that correlate with the enhanced electronic properties were investigated to provide detailed insight into how these relate. GIWAXS profiles for **P1** films slow-dried in CHCl<sub>3</sub> show well-defined higher-order out-of-plane diffraction peaks (200) at  $q \approx 0.54$  Å<sup>−1</sup> and (300) at  $q \approx 0.86$  Å<sup>−1</sup>, indicating improved lamellar side-chain stacking (Figure 4a). Additionally, backbone stacking is enhanced, as observed from the emergence of sharper and narrower diffraction peaks (001) at  $q \approx 0.51$  Å<sup>−1</sup> ( $d \approx 12.32$  Å) and (002) at  $q \approx 1.04$  Å<sup>−1</sup> in the out-of-plane direction, for **P1** films slow-dried in CHCl<sub>3</sub> and hexanes (Figure 4a–c).<sup>[41]</sup> **P1** films slow-dried in CHCl<sub>3</sub> show additional peaks (001)' at  $q \approx 0.35$  Å<sup>−1</sup> ( $d \approx 17.95$  Å) and (002)' at  $q \approx 0.68$  Å<sup>−1</sup> in the out-of-plane direction. The backbone scattering is indicative of exceptionally high backbone rigidity compared to other high mobility polymers, which can be associated with a reduction in disorder-induced localization, lower  $E_a$ , and enhanced  $\mu$ .<sup>[42]</sup> Furthermore, several in-plane peaks associated with polymorphs arise at  $q \approx 1.20$ – $1.50$  Å<sup>−1</sup>. Polymorph structures have demonstrated enhanced interchain charge transport between complex molecular packing features/structures.<sup>[43,44]</sup> The existence of (010) diffraction peaks at  $1.65$  Å<sup>−1</sup> in the out-of-plane direction indicates that **P1** adopts a face-on orientation with a  $\pi$ – $\pi$  spacing of  $\approx 3.81$  Å regardless

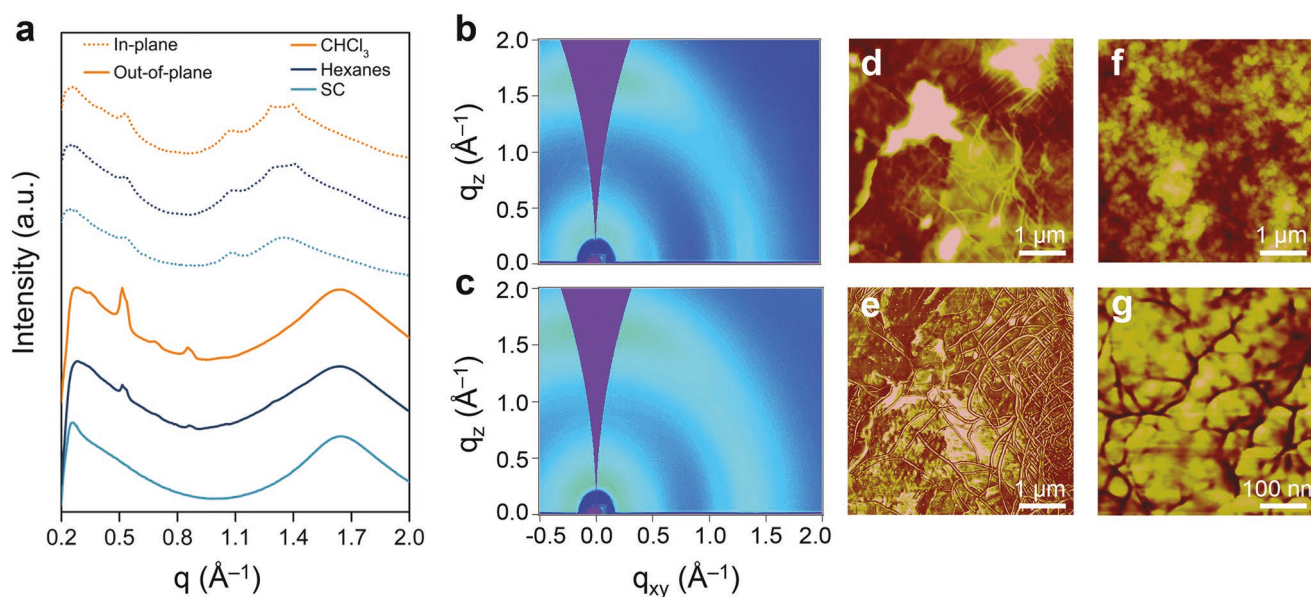


**Figure 4.** Morphological comparison of slow-dried **P1** films. a) 1D line cuts of the integrated in-plane and out-of-plane GIWAXS profiles for **P1** films cast using different processing conditions. The corresponding 2D GIWAXS profiles for films b) slow-dried in  $\text{CHCl}_3$  and c) slow-dried in hexanes. AFM d,f) height and e,g) phase images of **P1** films slow-dried in  $\text{CHCl}_3$  (comprising fibrous structures) and hexanes (yielding granular textures with clear grain boundaries), respectively.

of the processing conditions. No strong  $\pi$ - $\pi$  stacking features are present for **P2** and **P3** under any conditions, however, these materials show a similar trend in the evolution of their lamellar side-chain packing and backbone stacking (Figure S12, Supporting Information). The decrease in the intensity of backbone scattering (001) and (001)' peaks in going from **P1**  $\rightarrow$  **P2**  $\rightarrow$  **P3** is indicative of a less rigid backbone or reduction of ordered phases. Key parameters determined from GIWAXS measurements for **P1**–**P3** are tabulated in Table S4 (Supporting Information). Although GIWAXS suggests a very similar enhancement in order, AFM measurements show dramatic differences in the morphology with nanoscale fibrillar structures present in the high performing **P1** films slow-dried in  $\text{CHCl}_3$  with RMS roughness of 23.1 nm (Figure 4d,e). The fibers, likely comprised of bundles of well-ordered polymer chains, are directionally random with lengths surpassing the micrometer scale and an average diameter of  $\approx 49$  nm. Similar structures have been shown to possess higher molecular ordering, the absence of grain boundaries, and enhanced transport.<sup>[39,45]</sup> As seen in Figure 4f,g, **P1** films slow-dried in hexanes adopt a more granular texture and a rough surface (RMS roughness = 25.8 nm) with clear grain boundaries between domains. This morphology creates trapping sites consistent with a reduction in  $\mu$  ( $3.93 \times 10^{-4} \text{ cm}^2 \text{ V}^{-1} \text{ s}^{-1}$ ), higher  $E_a$  of 298 meV, and lower  $\sigma_{\text{RT}}$  of  $1.91 \times 10^{-5} \text{ S cm}^{-1}$ .<sup>[46]</sup> A comparison of these results with **P2** and **P3** films is helpful in elucidating structural and morphological parameters relevant to charge transport. The absence of well-defined  $\pi$ - $\pi$  stacking in **P2** and **P3** films suggests that this is a requisite for fiber formation (Figure S13, Supporting Information). **P2** and **P3** films slow-dried in  $\text{CHCl}_3$  present similar aggregates to their spin-coated counterparts, but with larger diameters of 10–20 and 40–50 nm, respectively. We attribute this change to improved polymer chain interactions, as suggested

by the presence of backbone scattering in GIWAXS profiles (Figure S12, Supporting Information) and the promotion of more extensive aggregation from the slow-drying process. These results agree with the approximately tenfold enhancement in  $\sigma_{\text{RT}}$  for both **P2** and **P3** when compared to spin-coated films (Figure 3a). The lower  $\sigma_{\text{RT}}$  and  $\mu$  obtained for all polymer films slow-dried in hexanes can be attributed to the presence of clear grain boundaries, in which there is an absence of inter-connecting chains that traverse disordered phases and link the domains. Furthermore, slow-drying in hexanes results in more coarse morphologies for **P2** and **P3** (RMS roughness = 1.84 and 57.4 nm, respectively), further impeding carrier transport (Figure S13, Supporting Information). The absence of fibrous structures limits charge transport within the **P2** and **P3** films.

Using an improved synthetic route and straightforward slow-drying process, **P1** demonstrates a record high  $\sigma_{\text{RT}}$  of  $8.18 \text{ S cm}^{-1}$  for a charge-neutral, undoped material. We benchmarked this value with other neutral narrow bandgap conjugated polymers,<sup>[16,47–50]</sup> polysquaraines,<sup>[14,51]</sup> radical polymers,<sup>[1,52,53]</sup> self-doped polyelectrolytes,<sup>[54–56]</sup> and some commercial grades of poly(styrene-sulfonate)-doped poly(3,4-ethylenedioxythiophene) (PEDOT:PSS) (Figure 5 and Figure S18 (Supporting Information)),<sup>[11]</sup> with full details assembled in Table S5 (Supporting Information). Neutral narrow bandgap polymers based on quinoidal poly(isothianaphthene) frameworks achieve  $\sigma \approx 10^{-3}$ – $10^{-2} \text{ S cm}^{-1}$ , while the highest performing captodatively stabilized zwitterionic polysquaraines achieve  $\sigma \approx 10^{-4} \text{ S cm}^{-1}$ . Neutral radical polymers exhibit  $\sigma \approx 10^{-5}$ – $10^{-1} \text{ S cm}^{-1}$ . Commercial grades of PEDOT:PSS with comparative  $\sigma_{\text{RT}}$  to **P1**–**P3** include Clevios P VP CH 8000 ( $\sigma \approx 10^{-6}$ – $10^{-5} \text{ S cm}^{-1}$ ), Clevios P VP AI 4083 ( $\sigma \approx 10^{-4}$ – $10^{-3} \text{ S cm}^{-1}$ ), and Clevios P ( $\sigma \approx 0.2$ – $1 \text{ S cm}^{-1}$ ). We also monitored the stability of high performing **P1** films slow-dried in  $\text{CHCl}_3$  under

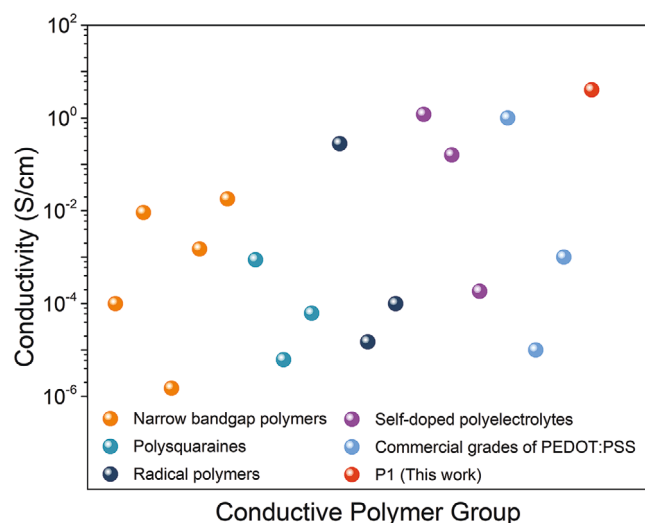


**Figure 5.** A comparison of the electrical conductivity of high performing **P1** films benchmarked against neutral narrow bandgap, self-doped, radical, and commercial conductive polymers. **P1** demonstrates a record high  $\sigma_{RT}$  of  $8.18 \text{ S cm}^{-1}$  for a polymer in its native “undoped” form. Commercial grades of PEDOT:PSS with comparable conductivities are included for comparison purposes.

various conditions. Films stored and measured under an inert atmosphere and in ambient conditions, both in the presence and absence of light, showed no discernable changes in conductivity over a period of 60 days (Figure S14, Supporting Information).

### 3. Conclusions

The functionality of these macromolecules demonstrates an intimate connection between chemical and electronic structure, solid-state microstructure, and hierarchical order that, while unique, draws many analogies to leading bodies of literature and design principles for organic semiconductors, conductive polymers, and radical conductors. Conductivity without doping is a result of narrow bandgaps and open-shell structures with greater spin and  $\pi$ -delocalization than previous classes of materials with unpaired electrons. The improved synthesis of these materials was essential to achieve high purity, high molecular weight, and enhanced molecular order. In these high molecular weight rigid-rod polymers,  $\pi$ - $\pi$  stacking in the ordered phases, backbone rigidification, and long-range alignment are important to achieving more favorable charge transport. Processing critically affects electronic coupling, film microstructure, mesoscopic domain organization, and bulk electronic properties. The subtle interplay between structure, morphology, and electronic properties is reminiscent of prototypical organic semiconductors; while, the narrow bandgaps, open-shell structures, strong electron correlations, solution processability, and robust stability offer new opportunities for the transport of charge in molecular systems. We anticipate that significant improvements can be made, considering these very preliminary results and that new optoelectronic functionalities and devices can be realized.

### 4. Experimental Section

Experimental details and additional characterization data are included in the Supporting Information.

### Supporting Information

Supporting Information is available from the Wiley Online Library or from the author.

### Acknowledgements

The work performed at The University of Southern Mississippi was supported by the US Army Engineer Research and Development Center (ERDC) under PE 0603734A, Project T15, Task “Advanced Polymer Development” under Grant No. ERDC BAA 18-0500 “Multifunctional Materials to Address Military Engineering” executed under Contract No. W912HZ-18-C-0022, and the National Science Foundation (Grant Nos. OIA-1757220 and NSF OIA-1632825). Permission to publish was granted by the Director, Geotechnical and Structures Laboratory. S.Z. and X.G. acknowledge support from the U.S. Department of Energy, Office of Science, Office of Basic Energy Sciences under Award Number DE-SC0019361. Use of the Stanford Synchrotron Radiation Lightsource, SLAC National Accelerator Laboratory, was supported by the U.S. Department of Energy, Office of Science, Office of Basic Energy Sciences under Contract No. DE-AC02-76SF00515. The EPR measurements at the University of Alabama were supported by the National Science Foundation (Grant No. CHE-1416238). A.B. and E.R.K. acknowledge traineeship support from the NSF NRT program “Interface” (Grant No. DGE-1449999) through the University of Southern Mississippi. M.M.L. thanks support from a University of Alabama Graduate Council Fellowship. M.K.B. was partially supported by the Ministry of Science and Education of the Russian Federation (Grant No. 14.W03.31.0034) and thanks A. G. Maryasov and O. A. Krumkacheva for helpful discussions. M.S. acknowledges the support from the U.S. Department of Energy, Office of Basic Sciences (Grant No. DE-SC0002136).

### Conflict of Interest

The authors declare no conflict of interest.

### Keywords

charge transport, conducting polymers, conjugated polymers, nanostructures, self-assembly

Received: November 24, 2019

Revised: February 28, 2020

Published online:

- [1] Y. Joo, V. Agarkar, S. H. Sung, B. M. Savoie, B. W. Boudouris, *Science* **2018**, 359, 1391.
- [2] S. K. Pal, M. E. Itkis, F. S. Tham, R. W. Reed, R. T. Oakley, R. C. Haddon, *Science* **2005**, 309, 281.
- [3] T. Kubo, A. Shimizu, M. Sakamoto, M. Uruichi, K. Yakushi, M. Nakano, D. Shiomi, K. Sato, T. Takui, Y. Morita, K. Nakasuji, *Angew. Chem., Int. Ed.* **2005**, 44, 6564.
- [4] T. M. Swager, *Macromolecules* **2017**, 50, 4867.

- [5] Z. Yang, J. Ren, Z. Zhang, X. Chen, G. Guan, L. Qiu, Y. Zhang, H. Peng, *Chem. Rev.* **2015**, 115, 5159.
- [6] D. S. Hecht, L. Hu, G. Irvin, *Adv. Mater.* **2011**, 23, 1482.
- [7] S. Mukherjee, B. W. Boudouris, *Organic Radical Polymers: New Avenues in Organic Electronics*, Springer International Publishing, New York **2017**.
- [8] K. Lee, S. Cho, S. H. Park, A. J. Heeger, C. W. Lee, S. H. Lee, *Nature* **2006**, 441, 65.
- [9] O. Bubnova, Z. U. Khan, H. Wang, S. Braun, D. R. Evans, M. Fabretto, P. Hojati-Talemi, D. Dagnelund, J. B. Arlin, Y. H. Geerts, S. Desbief, D. W. Breiby, J. W. Andreasen, R. Lazzaroni, W. M. Chen, I. Zozoulenko, M. Fahlman, P. J. Murphy, M. Berggren, X. Crispin, *Nat. Mater.* **2014**, 13, 190.
- [10] I. Salzmann, G. Heimel, M. Oehzelt, S. Winkler, N. Koch, *Acc. Chem. Res.* **2016**, 49, 370.
- [11] H. Shi, C. C. Liu, Q. L. Jiang, J. K. Xu, *Adv. Electron. Mater.* **2015**, 1, 1500017.
- [12] A. Elschner, S. Kirchmeyer, W. Lovenich, U. Merker, K. Reuter, *PEDOT: Principles and Applications of an Intrinsically Conductive Polymer*, CRC Press, Boca Raton **2010**.
- [13] X. Wang, X. Zhang, L. Sun, D. Lee, S. Lee, M. Wang, J. Zhao, Y. Shao-Horn, M. Dinca, T. Palacios, K. K. Gleason, *Sci. Adv.* **2018**, 4, eaat5780.
- [14] A. Ajayaghosh, *Chem. Soc. Rev.* **2003**, 32, 181.
- [15] J. Roncali, *Chem. Rev.* **1997**, 97, 173.
- [16] T. L. Dexter Tam, C. K. Ng, S. L. Lim, E. Yildirim, J. Ko, W. L. Leong, S.-W. Yang, J. Xu, *Chem. Mater.* **2019**, 31, 8543.
- [17] K. Oyaizu, H. Nishide, *Adv. Mater.* **2009**, 21, 2339.
- [18] M. E. Itkis, X. Chi, A. W. Cordes, R. C. Haddon, *Science* **2002**, 296, 1443.
- [19] S. K. Pal, M. E. Itkis, F. S. Tham, R. W. Reed, R. T. Oakley, B. Donnadieu, R. C. Haddon, *J. Am. Chem. Soc.* **2007**, 129, 7163.
- [20] G. E. Rudebusch, J. L. Zafra, K. Jorner, K. Fukuda, J. L. Marshall, I. Arrechea-Marcos, G. L. Espejo, R. P. Ortiz, C. J. Gomez-Garcia, L. N. Zakharov, M. Nakano, H. Ottosson, J. Casado, M. M. Haley, *Nat. Chem.* **2016**, 8, 753.
- [21] W. D. Zeng, H. Phan, T. S. Heng, T. Y. Gopalakrishna, N. Aratani, Z. B. Zeng, H. Yamada, J. Ding, J. S. Wu, *Chem* **2017**, 2, 81.
- [22] M. Abe, *Chem. Rev.* **2013**, 113, 7011.
- [23] G. Z. Magda, X. Jin, I. Hagymasi, P. Vancso, Z. Osvath, P. Nemes-Incze, C. Hwang, L. P. Biro, L. Tapasztó, *Nature* **2014**, 514, 608.
- [24] P. Ruffieux, S. Wang, B. Yang, C. Sanchez-Sanchez, J. Liu, T. Dienel, L. Talirz, P. Shinde, C. A. Pignedoli, D. Passerone, T. Dumslaff, X. Feng, K. Müllen, R. Fasel, *Nature* **2016**, 531, 489.
- [25] Y. Morita, S. Suzuki, K. Sato, T. Takui, *Nat. Chem.* **2011**, 3, 197.
- [26] Y. Joo, L. Huang, N. Eedugurala, A. E. London, A. Kumar, B. M. Wong, B. W. Boudouris, J. D. Azoulay, *Macromolecules* **2018**, 51, 3886.
- [27] A. E. London, H. Chen, M. A. Sabuj, J. Tropp, M. Saghayezhian, N. Eedugurala, B. A. Zhang, Y. Liu, X. Gu, B. M. Wong, N. Rai, M. K. Bowman, J. D. Azoulay, *Sci. Adv.* **2019**, 5, eaav2336.
- [28] J. D. Yuen, M. F. Wang, J. Fan, D. Sheberla, M. Kemei, N. Banerji, M. Scarongella, S. Valouch, T. Pho, R. Kumar, E. C. Chesnut, M. Bendikov, F. Wudl, *J. Polym. Sci., Part A: Polym. Chem.* **2015**, 53, 287.
- [29] Y. Li, L. Li, Y. Wu, Y. Li, *J. Phys. Chem. C* **2017**, 121, 8579.
- [30] M. Li, C. An, W. Pisula, K. Müllen, *Acc. Chem. Res.* **2018**, 51, 1196.
- [31] Z. B. Henson, K. Müllen, G. C. Bazan, *Nat. Chem.* **2012**, 4, 699.
- [32] L. Ying, B. B. Hsu, H. Zhan, G. C. Welch, P. Zalar, L. A. Perez, E. J. Kramer, T. Q. Nguyen, A. J. Heeger, W. Y. Wong, G. C. Bazan, *J. Am. Chem. Soc.* **2011**, 133, 18538.
- [33] K. Susumu, T. V. Duncan, M. J. Therien, *J. Am. Chem. Soc.* **2005**, 127, 5186.
- [34] T. Cai, Y. Zhou, E. Wang, S. Hellström, F. Zhang, S. Xu, O. Inganäs, M. R. Andersson, *Sol. Energy Mater. Sol. Cells* **2010**, 94, 1275.
- [35] K. Wang, L. Huang, N. Eedugurala, S. Zhang, M. A. Sabuj, N. Rai, X. Gu, J. D. Azoulay, T. N. Ng, *Adv. Energy Mater.* **2019**, 9, 1902806.
- [36] H. Zhang, H. Dong, Y. Li, W. Jiang, Y. Zhen, L. Jiang, Z. Wang, W. Chen, A. Wittmann, W. Hu, *Adv. Mater.* **2016**, 28, 7466.
- [37] H. N. Tsao, D. Cho, J. W. Andreasen, A. Rouhanipour, D. W. Breiby, W. Pisula, K. Müllen, *Adv. Mater.* **2009**, 21, 209.
- [38] S. Schott, U. Chopra, V. Lemaure, A. Melnyk, Y. Olivier, R. Di Pietro, I. Romanov, R. L. Carey, X. C. Jiao, C. Jellett, M. Little, A. Marks, C. R. McNeill, I. McCulloch, E. R. McNellis, D. Andrienko, D. Beljonne, J. Sinova, H. Sirringhaus, *Nat. Phys.* **2019**, 15, 814.
- [39] S. Wang, M. Kappl, I. Liebewirth, M. Müller, K. Kirchhoff, W. Pisula, K. Müllen, *Adv. Mater.* **2012**, 24, 417.
- [40] G. Tan, L. D. Zhao, M. G. Kanatzidis, *Chem. Rev.* **2016**, 116, 12123.
- [41] Z. Fei, Y. Han, E. Gann, T. Hodsden, A. S. R. Chesman, C. R. McNeill, T. D. Anthopoulos, M. Heeney, *J. Am. Chem. Soc.* **2017**, 139, 8552.
- [42] D. Venkateshvaran, M. Nikolka, A. Sadhanala, V. Lemaure, M. Zelazny, M. Kepa, M. Hurhangee, A. J. Kronemeijer, V. Pecunia, I. Nasrallah, I. Romanov, K. Broch, I. McCulloch, D. Emin, Y. Olivier, J. Cornil, D. Beljonne, H. Sirringhaus, *Nature* **2014**, 515, 384.
- [43] Y. Yuan, G. Giri, A. L. Ayzner, A. P. Zoombelt, S. C. Mannsfeld, J. Chen, D. Nordlund, M. F. Toney, J. Huang, Z. Bao, *Nat. Commun.* **2014**, 5, 3005.
- [44] H. R. Tseng, L. Ying, B. B. Hsu, L. A. Perez, C. J. Takacs, G. C. Bazan, A. J. Heeger, *Nano Lett.* **2012**, 12, 6353.
- [45] S. Wang, L. Dossel, A. Mavrinskiy, P. Gao, X. Feng, W. Pisula, K. Müllen, *Small* **2011**, 7, 2841.
- [46] H. R. Tseng, H. Phan, C. Luo, M. Wang, L. A. Perez, S. N. Patel, L. Ying, E. J. Kramer, T. Q. Nguyen, G. C. Bazan, A. J. Heeger, *Adv. Mater.* **2014**, 26, 2993.
- [47] H. L. Gao, C. W. Ge, B. Hou, H. S. Xin, X. K. Gao, *ACS Macro Lett.* **2019**, 8, 1360.
- [48] E. Staes, D. Vangeneugden, L. J. Nagels, D. Vanderzande, J. Gelan, *Electroanalysis* **1999**, 11, 65.
- [49] T.-A. Chen, R. D. Rieke, *Synth. Met.* **1993**, 60, 175.
- [50] Y. Ikenoue, F. Wudl, A. J. Heeger, *Synth. Met.* **1991**, 40, 1.
- [51] J. Eldo, A. Ajayaghosh, *Chem. Mater.* **2002**, 14, 410.
- [52] L. Rostro, S. H. Wong, B. W. Boudouris, *Macromolecules* **2014**, 47, 3713.
- [53] M. E. Hay, S. H. Wong, S. Mukherjee, B. W. Boudouris, *J. Polym. Sci., Part B: Polym. Phys.* **2017**, 55, 1516.
- [54] C. K. Mai, R. A. Schlitz, G. M. Su, D. Spitzer, X. Wang, S. L. Fronk, D. G. Cahill, M. L. Chabinyc, G. C. Bazan, *J. Am. Chem. Soc.* **2014**, 136, 13478.
- [55] C. K. Mai, H. Zhou, Y. Zhang, Z. B. Henson, T. Q. Nguyen, A. J. Heeger, G. C. Bazan, *Angew. Chem., Int. Ed.* **2013**, 52, 12874.
- [56] J. W. Jo, J. W. Jung, S. Bae, M. J. Ko, H. Kim, W. H. Jo, A. K. Y. Jen, H. J. Son, *Adv. Mater. Interfaces* **2016**, 3, 1500703.